

Capturing Fingerprints of Conical Intersection: Complementary Information of Non-Adiabatic Dynamics from Linear X-ray Probes

Deependra Jadoun, Mahesh Gudem, and Markus Kowalewski*

Department of Physics, Stockholm University, Albanova University Centre, SE-106 91 Stockholm, Sweden

(Dated: March 19, 2022)

Many recent experimental ultrafast spectroscopy studies have hinted at non-adiabatic dynamics indicating the existence of conical intersections, but their direct observation remains a challenge. The rapid change of the energy gap between the electronic states complicated their observation by requiring bandwidths of several electron volts. In this manuscript, we propose to use the combined information of different X-ray pump-probe techniques to identify the conical intersection. We theoretically study the conical intersection in pyrrole using transient X-ray absorption, time-resolved X-ray spontaneous emission, and linear off-resonant Raman spectroscopy to gather evidence of the curve crossing.

Keywords: X-ray Spectroscopy, Conical Intersections, Time-Resolved Spectroscopy, Quantum Dynamics

I. INTRODUCTION

Conical intersections (CIs) [1–3], though once considered rare, govern the outcome of many of the photochemical reactions, according to modern photochemistry [4–6]. They appear in a molecule when two or more potential energy surfaces (PESs) cross and enable the possibility of electronic de-excitation without radiative emission. These non-radiative transitions result in the breakdown of the Born-Oppenheimer approximation. Consequently, the electronic and nuclear degrees of freedom are strongly coupled in the vicinity of the CI. It is now well established that the CIs play a vital role in several photochemical processes such as photosynthesis [7], primary event of vision [8], photochemical formation of DNA lesions [9], and photochemistry of individual nucleobases [10]. However, the direct experimental detection of CIs in molecular systems is still challenging. This is mainly because the energy gap between PESs near the CI decreases rapidly. Ultrashort pulses with adequate resolution in both energy and time domain are required to observe them.

With the advent of X-ray lasers, it is possible to probe such fast processes that occur on the timescale of femtoseconds and attoseconds using ultrafast pump-probe spectroscopy [11–21]. It has been recently shown experimentally that attosecond transient absorption spectroscopy (ATAS) can aid the observation of non-adiabatic processes [22–25]. Time-resolved photoelectron spectroscopy [26, 27], and X-ray diffraction [28] have also been proposed to study the behaviour of system in the vicinity of a CI.

Spectroscopic techniques that involve attosecond pulses provide a high resolution in the time-domain, and cover a broad range of frequencies, making them a

promising tool to measure the rapidly varying energy gap that comes with CIs. However, their experimental availability can be a limiting factor.

In the following, we show theoretically how a combination of femtosecond based X-ray probe methods may be used to detect the non-adiabatic dynamics in a molecule. Our chosen example molecule, pyrrole, exhibits a CI in the photodissociation pathway of the hydrogen atom. The branching ratio between the electronic states in the vicinity of the CI is on the order of a few percent, making it a rather challenging example [29]. The goal of the present work is to show that it is possible to locate a CI even when there is an unbalanced branching of the electronic state population in its vicinity, using widely used femtosecond X-ray probe methods. A purely diabatic or purely adiabatic population transfer poses a challenge for spectroscopic X-ray techniques to identify the existence of the second electronic state involved in the CI. Three different techniques have been employed to study the photo dynamics of pyrrole involving a CI between ground and excited electronic state. The methods used here are as follows, time-resolved X-ray absorption spectroscopy (XAS), X-ray spontaneous emission spectroscopy (XSES) and recently proposed technique, transient redistribution of ultrafast electronic coherence in attosecond Raman signals (TRUECARS). We briefly introduce the features of the methods used in this manuscript in the following.

In the case when there is an unbalanced branching, one needs to look for the indirect signatures of a CI to detect its occurrence. We construct the transient XAS spectrum using femtosecond X-ray probe-pulses to observe the change in transition dipole-moment in the vicinity of a CI in pyrrole. Femtosecond pulses are sufficiently narrow in the frequency domain (≤ 1 eV, as compared to attosecond pulses) to selectively probe the transitions which are distributed over a few electron volts. The intensity of the XAS signal depends on the valence-to-core transition dipole moments that the

* E-mail: markus.kowalewski@fysik.su.se

probe pulse is resonant with, as well as the population of the valence states. It is possible to construct XAS spectra using attosecond pulses, but it may contain signatures originating from other resonant valence-to-core transitions, further complicating the interpretation of the spectrum.

Time-resolved XSES [30, 31] does not solely depend upon the branching of the wave packet and may provide additional information about the curve crossing. In the XSES spectrum, the energy gap in the vicinity of the CI may be observed directly independent of the population of the involved valence states and is expected to yield information about the shape of the PESs involved. In time-resolved XSES, pyrrole is excited to a nitrogen 1s core-hole state, which is followed by the spontaneous emission of a photon. The 1s core-hole states of nitrogen have a lifetime of 7 fs [32–34], and the spontaneous emission takes place within this time period after excitation.

Probing the creation of electronic coherences in the vicinity of CI provides a more direct signature of CIs. Several X-ray based spectroscopic techniques have been proposed theoretically to observe this phenomena [27, 35–37]. One such scheme is TRUECARS [38–40], which is based on an off-resonant linear Raman process. In this scheme, a hybrid probe-pulse sequence is used instead of a single probe pulse to construct the signal where the redistribution of photons maps out the time varying energy gap via the Raman shift. TRUECARS is only sensitive to the coherences and is thus expected to yield accurate information about the passage through the CI. However, to obtain the maximum intensity in the signal, a balanced branching at the CI is required. The result from TRUECARS signal can be considered confirmation for the other two methods. The use of hybrid pulses in TRUECARS and homodyne detection scheme makes it experimentally more challenging, whereas XAS and XSES have been used successfully earlier in experiments to study photochemical processes [41, 42].

We show that the three methods deliver complementary information that can be used to observe the direct (generation of vibronic coherence and state resolved spectra) and indirect (change in the transition dipole moments) effects of a CI between two states in the pyrrole molecule. The paper is structured as follows: section II presents the details of the system used for the signal calculations. In section III, the analytical expressions for spectroscopic signals and Hamiltonian for the various pump-probe methods are discussed. Section IV contains the details about the software and programs used to carry out the simulations. In section V, spectra calculated using different pump-probe methods are presented along with the discussion. Finally, the main conclusions drawn by comparing the results from used methods are presented in section VI.

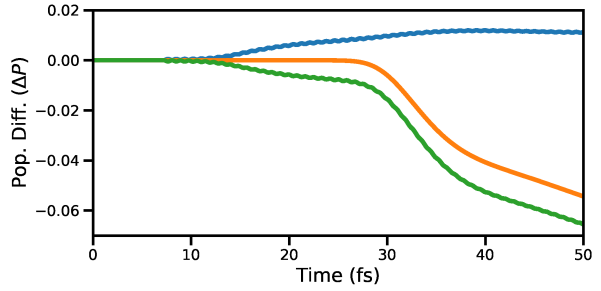


Figure 1. The plot shows the change in population ΔP after the pump-pulse ends for state S_0 (blue curve), state $\pi\sigma^*$ (green curve), and the total population of the system (orange curve). When the wave-packets reach the vicinity of CI around 10 fs, the population branches out, and consequently, the population for the $\pi\sigma^*$ starts to decrease, and the population for S_0 starts increasing. The system's total population starts to decay around 30 fs when the wave-packets hit the boundary of PES. The wave-packets are absorbed by the perfect-matched-layer placed at the edge of the PES.

II. MODEL

A. Photochemistry of pyrrole

Pyrrole is a nitrogen-containing five-membered heterocyclic aromatic compound, which has been used extensively as a model system for exploring non-adiabatic dynamics [29, 43–48]. The low-lying bright states of pyrrole emerge around 6 eV [49, 50]. It has been challenging to assign the corresponding peaks in ultra violet (UV) absorption spectrum. This is mainly due to the high density of energy levels lying around the bright states [51, 52].

The UV-induced photochemistry of pyrrole involves NH detachment process through the manifold of four lowest singlet excited states, $^1A_2(\pi\sigma^*)$, $^1B_1(\pi\sigma^*)$, $^1B_2(\pi\pi^*)$, and $^1A_1(\pi\pi^*)$ [29, 53]. The two $\pi\pi^*$ states have been assigned to the above-mentioned absorption bands around 6 eV. The molecules in these bright states undergo non-radiative decay to the $\pi\sigma^*$ states along the out-of-plane ring deformation coordinate [54]. The latter states have been found to be repulsive along the NH stretching mode [44, 55, 56]. The ring deformation mechanism was also shown to be feasible on the $\pi\sigma^*$ states [54]. Along the dissociation process, the ground state energy increases and forms a CI between S_0 and $\pi\sigma^*$ states [44]. The nature of the σ^* orbital was also shown to be varied during the detachment process. At the Franck-Condon (FC) geometry, it is of 3s Rydberg type which changes to valance σ^* upon NH stretching and eventually becomes a 1s orbital of the hydrogen atom. This Rydberg-to-valance orbital transformation rationalises the presence of the dissociation barrier on

the $\pi\sigma^*$ states [44]. The photodissociation dynamics of pyrrole involving $S_0/\pi\sigma^*(^1A_2$ and $^1B_1)$ CIs have been theoretically investigated by Domcke and co-workers [29]. The study employs the vertical excitation model and simulates the time-dependent dynamics of pyrrole on each $\pi\sigma^*$ state separately. Recently, optical cavities have been found to be hugely influencing the photolysis reaction dynamics in the $\pi\sigma^*(^1B_1)$ state [57]. The present work considers the photodynamics of pyrrole in the $\pi\sigma^*(^1B_1)$ state, referred to as just $\pi\sigma^*$ in the rest of the paper, as a model for the study. We have employed a simplified model by considering only the stretching coordinates corresponding to the NH bond. This reduced dimensionality model has been found to be describing the photofragmentation features of pyrrole qualitatively [29].

The main objective of the paper is to show how femtosecond based X-ray probe methods can be used to detect the CIs in molecular systems. Therefore, we include only S_0 and $\pi\sigma^*$ states, and the vibronic couplings of them with the other valence excited states have been neglected. These additional vibronic interactions [55, 56, 58, 59] and the other molecular modes like out-of-plane ring deformation [54], as mentioned above, may also play a role in describing the dissociation dynamics of pyrrole. Our model does not consider these effects. The treatment of all these couplings in an extended molecular mode space would be necessary for a fully quantitative description of the time-dependent photodissociation dynamics of pyrrole [54–56, 58, 59].

A detailed discussion on the PESs of valence states employed in the current work can be found in a recent study investigating the cavity-modified dynamics of pyrrole [57]. We provide the details very briefly here. Previous theoretical studies have established that the hydrogen elimination reaction dynamics in the $\pi\sigma^*$ state involves hydrogen in-plane and out-of-plane detachment motions [29, 57]. These coordinates, which will be denoted as R_1 and R_2 refer to the tuning and coupling coordinates, respectively. The computed PESs along the two reaction coordinates have been used to construct various spectroscopic signals from the quantum dynamics simulations. The valence states are considered to be in the diabatic basis. When the wave packets reach the CI, there is a diabatic population transfer (around 7% of population in excited state), mediated by the diabatic coupling between the states. The wave-packets on the $\pi\sigma^*$ state PES arrive in the vicinity of CI at around 10 fs and then starts to branch into S_0 , which can be seen in the population difference curves shown in Fig. 1 for S_0 state (blue curve) and $\pi\sigma^*$ state (green curve). The population difference for a particular state is calculated by subtracting the maximum population from the population at each time instance after the end of pump-pulse. The total population (orange curve) remains constant until the wave-packets reaches

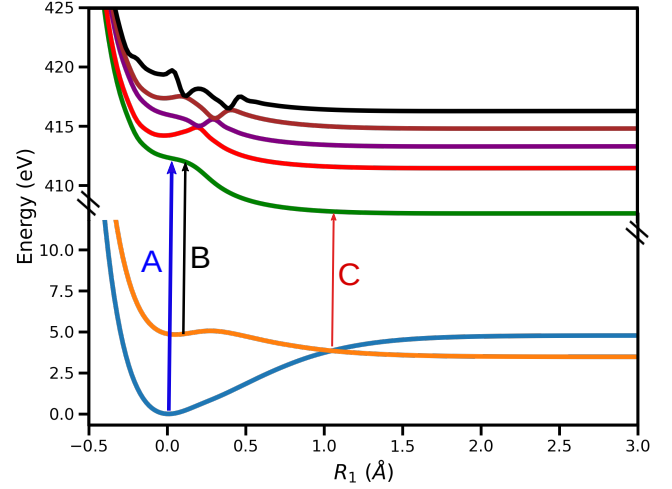


Figure 2. 1D cuts of the PESs of S_0 (blue), $\pi\sigma^*$ (orange) and five core-hole states (Nitrogen $1s$ core-hole states) of the pyrrole molecule. These curves show variation of the energy of the states along the reaction coordinate R_1 . The transitions from the valence-states to the first core-hole state C_1 are shown by various arrow. The transition between S_0 and C_1 , represented by A, has approximate energy of 412 eV. The transition represented by B between $\pi\sigma^*$ and C_1 has approximate energy of 407 eV [60] and transition corresponding to the CI region is denoted by C and has approximate energy of 404 eV.

the boundary of the PES and gets absorbed by perfectly matched layer [61]. To analyze the behavior of the system near CI, we use five core-hole states, which correspond to Nitrogen $1s$ orbital. The 1D strips of the PESs are shown in Fig. 2. The two valence states are denoted by S_0 and $\pi\sigma^*$ while the lowest core-hole state is denoted by C_1 .

B. Preparation of the system

A pump-probe scheme is used in the construction of the signals, as shown in Fig. 3. An UV pump-pulse is used to prepare the system by exciting it from the ground state (S_0) to the valence excited state ($\pi\sigma^*$) of the molecule.

The interaction of the molecule with the pump-pulse is included in the initial Hamiltonian, and the system after the interaction is called the prepared system. The Hamiltonian of the corresponding system can be written as,

$$\hat{H}_I = \hat{H}_0 + \hat{H}_U, \quad (1)$$

where \hat{H}_0 is the molecular Hamiltonian for the valence states, \hat{H}_U is the Hamiltonian which considers the effects of pump-pulse on the molecule under the dipole

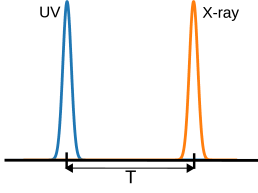


Figure 3. The schematic of the Pump-probe scheme used for the construction of signal. Here, T is the delay time between the pump and the probe pulse.

approximation. The molecular Hamiltonian and the interaction with UV pump-pulse reads:

$$\hat{H}_0 = \begin{bmatrix} \hat{T} + \hat{V}_0 & \hat{C}_{01} \\ \hat{C}_{01} & \hat{T} + \hat{V}_1 \end{bmatrix} \quad (2)$$

$$\hat{H}_U = -E_U \cdot \cos(\omega_U t) \cdot f_U(t) \begin{bmatrix} 0 & \hat{\mu}_{01} \\ \hat{\mu}_{10} & 0 \end{bmatrix} \quad (3)$$

In the Hamiltonian matrix in Eq. 2, \hat{T} and \hat{V} represent the kinetic energy operator and PES for a particular electronic state, respectively, and \hat{C}_{01} represents the diabatic couplings between the states S_0 and $\pi\sigma^*$. The reduced mass $m_r = 1809.5$ a.u. is used in the kinetic energy operator $T = (-1/2m_r)\nabla^2$, with ∇ being the gradient operator with respect to the reaction coordinates R_1 and R_2 . The V , C , and μ depend on the two reaction coordinates, R_1 and R_2 . In the Hamiltonian describing the interaction with the pump, $\hat{\mu}_{01}$ and $\hat{\mu}_{10}$ represent the transition dipole moments between S_0 and $\pi\sigma^*$ states. E_U represents the electric field strength of pump-pulse, ω_U is the carrier frequency of the pump-pulse and $f_U(t) = \exp(-t^2/2\sigma_U^2)$ is the Gaussian envelope of the laser pulse.

III. SPECTROSCOPIC SIGNALS

The expressions for the spectroscopic signals are discussed here, along with the modifications in Hamiltonian of the system. The electric field's effects from the pump pulse are calculated without any further approximation by including it in the system Hamiltonian (called prepared system) for all pump-probe signals.

A. X-ray Absorption Signal

In transient XAS, the absorption of an X-ray pulse, the interaction with a valence-to-core transition is recorded. The obtained spectrum contains information about the possible transitions. We note that photoelectrons can also be generated in a competing process. However, we neglect all the competing pathways and focus on the XAS signal. Here we have included the pump

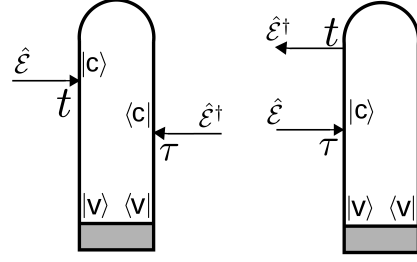


Figure 4. Loop diagrams corresponding to the XAS signal [62, 63]. The time runs along the loop from left bottom to right bottom. The interaction from left acts on the ket, and from the right acts on the bra. The arrows pointing inwards represent the absorption of the photon. The gray region defines the system prepared by the pump pulse, $|v\rangle$ represents the valence states, and $|c\rangle$ represents the core-hole states.

pulse in the Hamiltonian which creates the initial state (\hat{H}_I in Eq. 1). The interaction with the probe pulse is treated with time dependent perturbation theory. The total Hamiltonian can be written as follows,

$$\hat{H}(t) = \hat{H}_I + \hat{H}_{int}(t), \quad (4)$$

where $\hat{H}_{int}(t)$ is the interaction Hamiltonian representing the interaction between probe-pulse and the prepared system. Under the rotating wave approximation (RWA), the time-dependent interaction Hamiltonian is

$$\hat{H}_{int}(t) = \hat{\mathcal{E}}_X(t)\hat{\mu}_X^\dagger + \hat{\mathcal{E}}_X^\dagger(t)\hat{\mu}_X \quad (5)$$

with $\hat{\mu}_X$ ($\hat{\mu}_X^\dagger$) being the transition dipole operator for describing the valence-to-core transition and $\hat{\mathcal{E}}_X(t)$ is the electric field operator of the X-ray modes. The field state is considered to be a coherent state initially. The signal for the XAS spectrum is defined as the integrated rate of change of the number of photons as a function of the absorption frequency ω_s and a pump-probe delay T , and can be expressed as follows,

$$S(T, \omega_s) = \int_{-\infty}^{\infty} dt \frac{d\langle N_s \rangle}{dt} \quad (6)$$

with N_s being the photon number operator for the s th field-mode. The interaction Hamiltonian, $\hat{H}_{int}(t)$ in Eq. 4, appears in the signal expression as a consequence of the probe-pulse electric field $\hat{\mathcal{E}}_X$. The signal expression is then obtained by treating $\hat{H}_{int}(t)$ as the time-dependent perturbation. The expression then reads [27, 64–66],

$$S(T, \omega_s) = \frac{2}{\hbar^2} \mathcal{E}^*(\omega_s) \left[\int_{-\infty}^{\infty} e^{i\omega_s(t-T)} dt \right. \\ \left. \times \int_{-\infty}^{\infty} d\tau \mathcal{E}_0(\tau - T) e^{-i\omega_X(\tau-T)} C_S(t, \tau) \right] \quad (7)$$

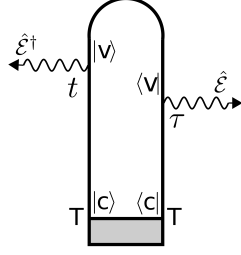


Figure 5. Loop diagram corresponding to the XSES. The gray region defines the interaction of system with pump-pulse as well as probe-pulse, and T is the time-delay between the pump-pulse and the probe-pulse.

where ω_X is the carrier frequency of the X-ray probe-pulse, $\mathcal{E}_0(t) = \exp(-t^2/2\sigma_X^2)$ is its Gaussian envelope, and ω_s is the frequency of the s th mode of the probe, and C_S is the correlation function which contains the information about the interaction between the probe-pulse and the system, for time instances τ and t as shown in Fig. 4.

$$C_S(t, \tau) = \langle \psi_0 | \hat{\mu}(t) \hat{\mu}^\dagger(\tau) | \psi_0 \rangle \quad (8)$$

where $|\psi_0\rangle$ represents the superposition of the wave functions that evolve on valence states of the molecule according to the prepared-system Hamiltonian \hat{H}_I . Note that Eq. 7 describes both, absorption and stimulated emission according to the diagrams in Fig. 4.

B. X-ray Spontaneous Emission Signal

The probe pulse of a particular center frequency is used to excite the system from the valence states to the core-hole states. The $1s$ core-hole states of Nitrogen in pyrrole have a lifetime of ≈ 7 fs [32–34] and hence spontaneous emission back to the valence states occurs on this time scale. To keep the computational effort tractable and stay within Hilbert space, we introduce the core-hole lifetime as an empirical parameter. Here we also neglect the photoionization due to the X-ray probe pulse as well as the subsequent Auger decay [67–69] and instead solely focus on spontaneous emission process. Note that the Auger process can be a dominant decay channel for relaxation from core excited states in light elements [70, 71]. The total Hamiltonian for constructing the XSES signal is similar to the Hamiltonian in Eq. 4. The difference is that now both the pump and probe pulses are included in the initial Hamiltonian, and the subsequent spontaneous emission process is treated with perturbation theory. The molecular Hamiltonian, the pump interaction, and probe in-

teraction are expressed as follows:

$$\hat{H}_0 = \begin{bmatrix} \hat{T} + \hat{V}_0 & \hat{C}_{01} & 0 \\ \hat{C}_{10} & \hat{T} + \hat{V}_1 & 0 \\ 0 & 0 & \hat{T} + \hat{V}_2 \end{bmatrix} \quad (9)$$

$$\hat{H}_U = -\mathbf{E}_U \cdot \cos(\omega_U t) \cdot f_U(t) \begin{bmatrix} 0 & \hat{\mu}_{01} & 0 \\ \hat{\mu}_{10} & 0 & 0 \\ 0 & 0 & 0 \end{bmatrix} \quad (10)$$

$$\hat{H}_X = -\mathbf{E}_X \cdot \cos(\omega_X t) \cdot f_X(t) \begin{bmatrix} 0 & 0 & \hat{\mu}_{02} \\ 0 & 0 & \hat{\mu}_{12} \\ \hat{\mu}_{20} & \hat{\mu}_{21} & 0 \end{bmatrix} \quad (11)$$

The notations in the molecular and pump field Hamiltonians are identical to the notation used in Eq. 2 and Eq. 3 with \hat{V}_2 being a core-hole state. In the probe field Hamiltonian matrix \hat{H}_X , $\hat{\mu}$'s represents the dipole moment between the valence (S_0 and $\pi\sigma^*$) and core-hole (C_1) states, $E_X = 2.06 \times 10^{11}$ V/m is the electric field strength of the probe pulse, ω_X is the carrier frequency of probe-pulse in X-ray regime, and $f_X(t) = \exp(-t^2/2\sigma_X^2)$ is the Gaussian envelope of the probe-pulse. The field operator of the spontaneously emitted photons takes the following form,

$$\hat{\mathcal{E}}(t) = \sum_s \left(\frac{2\pi\hbar\omega_s}{\Omega} \right)^{1/2} \hat{a}_s e^{-i\omega_s t} \quad (12)$$

where Ω is the quantization volume, and ω_s represents the frequency of the spontaneously emitted photon. The XSES signal is defined as the integrated rate of change of the number of photons as a function of the emission frequency ω_s and the pump-probe delay T . The signal expression then reads [72],

$$S(T, \omega_s) = -\frac{2}{\hbar\pi c^3} \Re \left[\int_{-\infty}^{\infty} dt \int_0^{\infty} \omega_s^3 d\omega_s \int_{-\infty}^t d\tau \times e^{i\omega_s(t-\tau)} e^{-\gamma t} C_E(\tau, t) \right] \quad (13)$$

where $\gamma = 1/\delta t$, with $\delta t = 7$ fs, is the decay rate for the core-hole states and C_E is the correlation function corresponding to the diagram shown in Fig. 5. The integral over the frequency ω_s is skipped in the final signal calculations as it is the variable for the frequency resolved detection. The two-time correlation function can be written as follows,

$$C_E(\tau, t) = \langle \psi_0(T) | \hat{\mu}^\dagger(\tau) \hat{\mu}(t) | \psi_0(T) \rangle, \quad (14)$$

where $|\psi_0(T)\rangle$ represents the C_1 state which is populated at the pump-probe delay T by X-ray pulse.

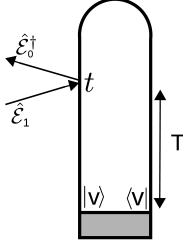


Figure 6. Loop diagram corresponding to the TRUECARs signal. The gray region defines the system prepared by the pump pulse, $|v\rangle$ represents the valence states, and T defines the time-delay between pump-pulse and the hybrid probe-pulses.

C. TRUECARs

In contrast to XAS and XSES, TRUECARs is a technique which is only sensitive to the vibronic coherences generated in the molecule. It uses a hybrid, off-resonant probe-pulse sequence. The signal consists of a Stokes and anti-Stokes type signal generated due to the redistribution of the photons between different modes. The TRUECARs spectrum is centered at the difference of the carrier frequencies of the hybrid probe pulses. The Raman shift indicates the energy difference between the involved valence states. Here we assume that the probe pulses have the same carrier frequency. The TRUECARs signal, which is constructed by perturbative treatment of the hybrid probe pulses, is represented by the following expression [38],

$$S(\omega_r, T) = 2\Im \int_{-\infty}^{\infty} dt e^{i\omega_r(t-T)} \mathcal{E}_0^*(\omega_r) \times \mathcal{E}_1(t-T) \langle \psi(t) | \hat{\alpha} | \psi(t) \rangle \quad (15)$$

where $\psi(t)$ is the linear combination of the valence-states wave function at the pump-probe delay T , ω_r is the Raman frequency, \mathcal{E}_0 and \mathcal{E}_1 are the two probe pulses respectively, and $\hat{\alpha}$ represents the polarizability tensor of the molecule [73]:

$$\hat{\alpha} = \begin{bmatrix} \alpha_{xx} & \alpha_{xy} & \alpha_{xz} \\ \alpha_{yx} & \alpha_{yy} & \alpha_{yz} \\ \alpha_{zx} & \alpha_{zy} & \alpha_{zz} \end{bmatrix} \quad (16)$$

where each element α_{ij} , with $i, j = x, y, z$ represents the directions of polarization. Each tensor element is expanded in the basis of the valence states:

$$\hat{\alpha}_{ij} = \begin{bmatrix} \alpha^{00} & \alpha^{01} \\ \alpha^{10} & \alpha^{11} \end{bmatrix} \quad (17)$$

Every element α^{kn} , with k, n representing the initial and final valence states, depends on the nuclear coordinates R_1 and R_2 , and the frequency of the probe-pulses

ω [73]:

$$\alpha_{ij}^{kn} = \frac{1}{\hbar} \sum_r \left(\frac{\mu_{i,kr} \mu_{j,rn}}{\omega_{rn} - \omega} + \frac{\mu_{i,rn} \mu_{j,kr}}{\omega_{rk} + \omega} \right) \quad (18)$$

where $\omega_{rn} = (E_r - E_n)/\hbar$ is the resonance frequency between the core-hole state r and the valence state n .

The matrix from Eq. 17 becomes non-Hermitian when Eq. 18 is used. Here we make the assumption that the energy difference between the valence states is small compared to $\omega_{rn} - \omega$ and the off-diagonal elements can be written as the average: $\alpha' = (\alpha^{01} + \alpha^{10})/2$. The new polarizability matrix, that is used in the calculations, then reads:

$$\hat{\alpha}'_{ij} = \begin{bmatrix} \alpha^{00} & \alpha' \\ \alpha' & \alpha^{11} \end{bmatrix}. \quad (19)$$

IV. METHODS

The ground state minimum structure of pyrrole, optimized at DFT/B3LYP/aug-cc-pVDZ level of theory, has been used as the reference geometry for computing the PESs. A rigid 2D-PES scan has been performed by employing the complete self-consistent field (CASSCF) method along with the aug-cc-pVDZ basis set. Three states have been included in the state-averaged CASSCF for calculating the PESs corresponding to the electronic valence states. The active space is comprised of seven orbitals (5 π -orbitals of ring and a pair of σ/σ^* -orbitals of NH bond) and 8 electrons. To compute the core excited state energies involving the electronic transition from the 1s-orbital of nitrogen atom, complete active space configuration interaction (CASSCF) method has been used. The prior-mentioned 3-state averaged CASSCF wave function, and the corresponding orbitals have been utilized to generate the configurations in the CASCI method. The diabatic PESs have been obtained using the quasi-diabatization procedure as implemented in MOLPRO-2019. The corresponding transformation matrix has been used to transform the dipole moments from adiabatic to diabatic basis. The program package MOLPRO-2019 [74, 75] has been used for the electronic structure calculations.

The correlation functions in Eqs. 8, 14, and 15 have been calculated by a direct propagation simulation protocol [76]. The wave packet dynamics have been calculated with our in-house software QDng. The Arnoldi method [77] was used to propagate the wave functions. The PESs and the numerical wave functions are represented on a grid with dimensions 256×256 . A perfectly matched layer is used to absorb the wave packets at the boundary of the numerical grid. The second derivative with respect to the reaction coordinates is calculated

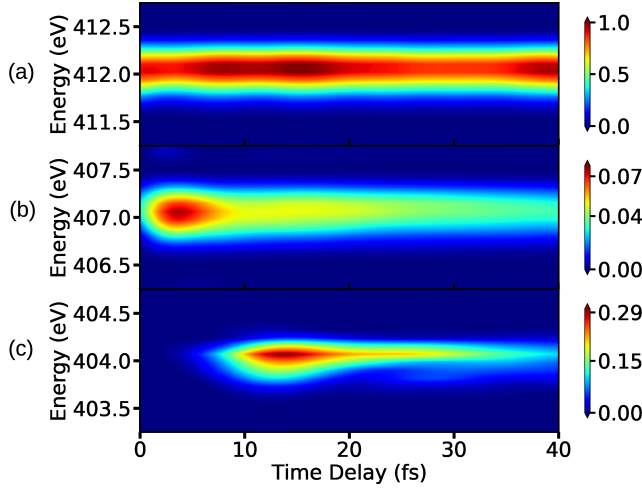


Figure 7. The XAS spectra for the lowest core-hole for X-ray center frequencies with (a) $\omega_X = 412$ eV, (b) $\omega_X = 407$ eV, and (c) $\omega_X = 404$ eV. The other UV pulse and X-ray pulse parameters used for the signal calculations are as follows: $E_U = 7.71 \times 10^{10}$ V/m, $\sigma_U = 1$ fs (FWHM = 2.35 fs), $\omega_U = 4.76$ eV, and $\sigma_X = 1.5$ fs (FWHM = 3.53 fs).

using the Fourier transform method. For all the propagations, a time step size of 50 as has been used. Since the lifetime of nitrogen 1s core-hole states is ≈ 7 fs, the time-evolution of the core-hole states in the XSES signal is done until 12.2 fs.

V. RESULTS AND DISCUSSION

The XAS signal is calculated by solving Eq. 7 for the core-hole states shown in Fig. 2. The C_1 state is energetically 3-4 eV apart from nearest core-hole state in the vicinity of the CI and thus the XAS signal is constructed only for the C_1 state. This can be used to distinguish the various features in the spectrum. The X-ray pulse has a finite width in the energy domain and thus the signal can be expected to show sharp features. Using an appropriate pulse-width and center-frequency of the X-ray pulse, it is possible to probe absorption bands belonging to different energy regimes as shown in Fig. 2. The signals are shown in Fig. 7 for three different X-Ray probe center frequencies, corresponding to transitions A, B and C in Fig. 2. Note that, when all the core-hole states are considered for the signal construction, the transitions corresponding to A and B for C_1 state will be resonant with transitions from other core-hole states as well. The XAS spectrum shown in Fig. 7(a) corresponds to the transition from state S_0 to state C_1 in the energy regime denoted by A in Fig. 2. The signal has almost constant intensity for all measured time-delays, while small variations in intensity originate

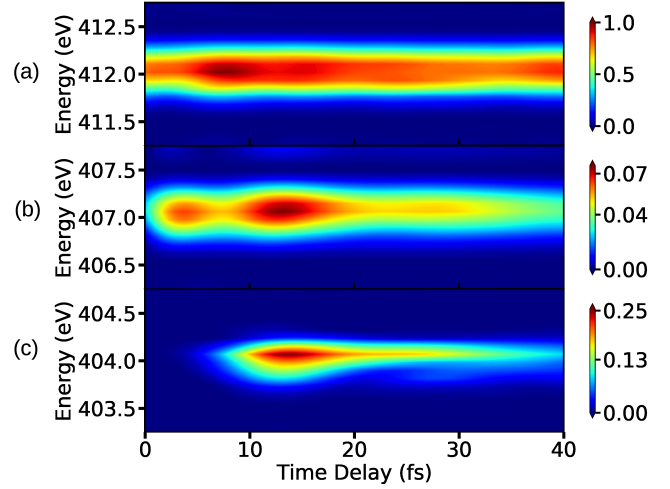


Figure 8. (a) The XAS spectra for five core-hole states for (a) $\omega_X = 412$ eV, (b) $\omega_X = 407$ eV and (c) $\omega_X = 404$ eV. The other pulse parameters for UV pulse and X-ray pulse are same as the ones used in Fig. 7. The bump in (b) appears because the CI region is resonant with C_2 for $\omega_X = 407$ eV, which was not present in Fig. 7(b).

from the pump pulse and the unbalanced branching ratio near the CI. We note that the signal shows similar features as the attosecond transient absorption spectroscopy spectrum recorded for the carbon K-edge in $C_2H_4^+$ to study the conical intersection between the D_0 and D_1 states [25]. This signal has higher intensity compared to signals corresponding to the transitions B and C in Fig. 2. The reason being the population residing at the local minima of S_0 state, as shown in Fig. 2, is higher than the population transferred to the $\pi\sigma^*$ state by the pump pulse. Hence the intensity of signal in Fig. 7(a) is used as a reference for signals corresponding to other energy regions. The signal shown in Fig. 7(b) correspond to the transition B in Fig. 2 and it has highest intensity when pump-pulse is about to vanish and the intensity decreases when the wave packets starts to move away from the FC point. The steady decrease in the intensity after some time indicates the presence of a local minima in the $\pi\sigma^*$ state. A certain amount of population is trapped in that minima that continues to leak over time. Figure 7(c) indicates that the absorption is taking place near the CI: the signals appears when the wave-packets on the $\pi\sigma^*$ state arrive in the vicinity of the CI and it vanishes when the wave-packets move past the CI region and move out of resonance with the probe-pulse. The transition from $\pi\sigma^*$ state to C_1 near the CI has a significantly higher intensity compared to transition between same states in the FC region (transition B in Fig. 2), and it can be observed by comparing Fig. 7(b) and Fig. 7(c). The increase in the intensity of signal near the CI indicates

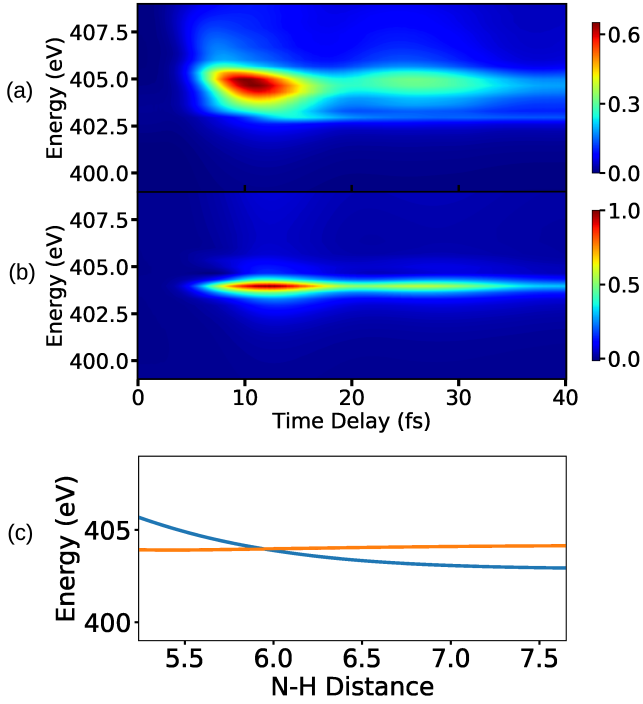


Figure 9. (a) The S_0 state contribution to the XSES spectrum for the C_1 state. (b) The $\pi\sigma^*$ state contribution to the XSES spectrum. (c) The separation between the S_0 and C_1 state (blue curve), and separation between $\pi\sigma^*$ and C_1 state (orange curve) as a function of one reaction coordinate for a fixed value of other reaction parameters is shown here. The UV pulse and X-ray pulse parameters used for the signal calculations are as follows: $E_U = 7.71 \times 10^{10}$ V/m, $\sigma_U = 1$ fs (FWHM = 2.35 fs), $\omega_U = 4.76$ eV, and $E_X = 2.06 \times 10^{11}$ V/m, $\sigma_X = 0.5$ fs (FWHM = 1.18 fs), $\omega_X = 403.3$ eV.

that the transition dipole-moment between the involved states increases in the vicinity of the CI. The fact that there are parts of the wave packets retained in the local minimum at the FC of the $\pi\sigma^*$ state supports the conclusion about increase in transition dipole-moment around CI. There is an increase in the intensity of the signal in Fig. 7(a), between 5 and 20 fs and around 40 fs, when the wave packets pass through the CI. It is a result of the transfer of low energy wave-packets from $\pi\sigma^*$ to the S_0 state near CI, that return to the minima of S_0 state. These vibrationally excited wave packets oscillate in the bounded region of the S_0 potential. Note that it is not possible to observe the change in the nature of the σ^* orbital along the dissociation coordinate in XAS spectrum. The X-ray probe frequency required to probe the transformation region is almost resonant with the absorption frequency of CI region. As a result the XAS signal from CI region dominates the XAS signal from the Rydberg-to-valence transformation region.

The XAS spectra shown in Fig. 8 contains the contri-

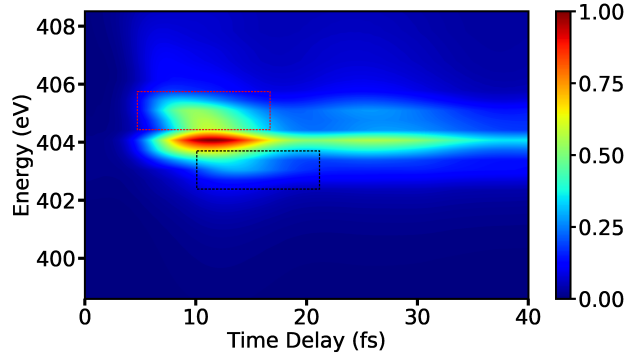


Figure 10. The total XSES spectrum for the C_1 state. The regions marked with red and black dotted boxes correspond to the S_0 state PES before and after the CI, respectively.

butions from five core-hole states. The non-adiabatic couplings between the core-hole states, which have avoided crossings, are not included in the calculations. The avoided crossings are spatially well separated from the CI between the valence states and thus it is expected that these crossings do not significantly alter the spectrum. When all five core-hole states (shown in Fig. 2) are used to construct the XAS signal, multiple valence-to-core transitions can be resonant with the same probe-pulse center-frequency. The transition C in Fig. 2 has the lowest energy and it is the only transition resonant with the probe pulse with a center frequency 404 eV. The number of resonant transitions increases by further increasing the carrier frequency.

The XAS signal corresponding to the transitions taking place in the vicinity of CI is shown in Fig. 8(c). Due to the resonance condition, signal in Fig. 8(c) has the same shape as the signal for a single core-hole state has in Fig. 7(c). The transition corresponding to the FC region for the $\pi\sigma^*$ state is resonant with the transition between the C_2 state and the CI region, and hence there is increase in intensity of the signal between 10 fs and 20 fs in Fig. 8(b). The overlap of multiple signals can also be seen in the Fig. 8(a) which correspond to the absorption from the S_0 state's local minimum. Since the intensity of the signal in Fig. 8(a) is used as a reference for other (Fig. 8(b) and (c)) signals, the spectrum in Fig. 8(c) has a lower intensity than the signal in Fig. 7(c). Apart from the change in peak intensity for absorption corresponding to 412 eV in Fig. 7 and 8, there is a noticeable difference between the shape of the signals as well. The increase of intensity in the XAS spectrum in Fig. 8(c) at around 8 fs, can be interpreted as an arrival of the wave packet in the CI region.

The XSES spectrum can be used to complement the findings from the XAS signal and to observe the energy gap between the valence states directly. The XSES spectrum is constructed by solving Eq. 13. For the sake

of clarity, the XSES signals are constructed for both S_0 and $\pi\sigma^*$ states separately. In the simulated spectra, the contribution to the total signal from each state can be evaluated.

The spectrum shown in Fig. 9(a) corresponds to the signal of the S_0 final state and it gets stronger when the wave packets approach the CI. The signal decays when the location of the wave packets is not resonant anymore with the probe pulse. This behavior follows a trend between 5 fs and 20 fs which corresponds to the blue curve in the Fig. 9(c) representing the separation between the S_0 state and the C_1 state as a function of a reaction coordinate. The signal that corresponds to the $\pi\sigma^*$ state is shown in Fig. 9(b) and the increase and decrease in intensity over the time shows a similar behavior as in the case of the S_0 state.

The change in intensity as a function of emission frequency and time delay in XSES spectra can be understood as follows: The spatial position of the wave packets on a PES relates them to a possible transition frequency for a particular state. If the energy of an excitation pulse is resonant or close to resonance for that transition frequency, the excitations will be maximum which would result in higher emission. Since the energy of the X-ray pulse is 403.3 eV, the signal will have the highest intensity when the wave packets reach the region before the CI which has resonance frequency of around 404 eV. For a specific delay, the strength of the signal would depend upon the transition dipole moment between the valence and core-hole states. Out of the two valence states, the $\pi\sigma^*$ state has higher amplitude of transition dipole-moment to the C_1 state and hence will have higher intensity of XSES signal.

As can be seen in Fig. 9(c), the separation between the $\pi\sigma^*$ state and the C_1 state is almost constant (represented by orange curve) and a similar feature is found in the XSES spectrum in Fig. 9(b). This indicates that the XSES may be able to project the relative shapes of the PESs of involved states. The total XSES spectrum which includes both the valence states is shown in the Fig. 10. The region shown in the red box corresponds to the S_0 state before the CI, and the region shown in the black box corresponds to the same state but after the CI. The signal in the black box starts to develop around 10 fs, which matches the time when the system reaches the CI as predicted by the XAS signal in Fig. 7. The valence states can be seen to approach each other before 10 fs and move apart subsequently.

Assuming that the transition dipole moments between the two valence states and the core-hole states are comparable to each other, the XSES signal can be used to detect the two PESs approaching each other before the CI and move apart after the CI. The only necessary condition is that the energy of the X-ray pulse should be resonant with the core-hole states in CI region.

We now discuss the TRUECARs spectrum. Figure

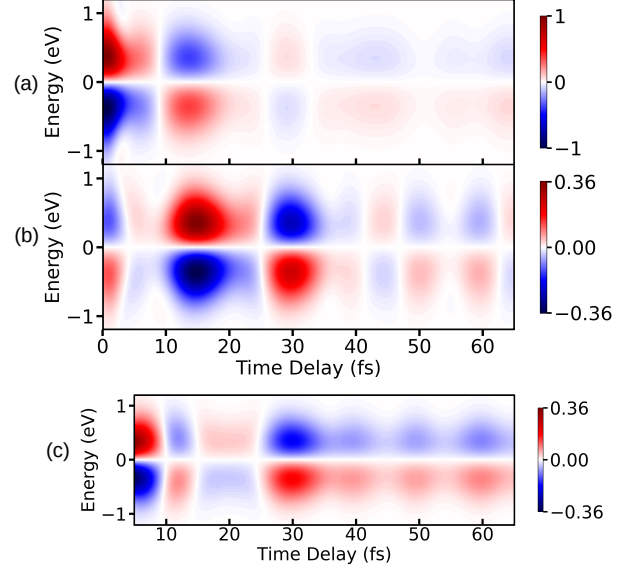


Figure 11. The TRUECARs spectra for (a) α_{xx} and (b) α_{yy} (c) $\alpha_{xx} + \alpha_{yy}$ are shown here. Note that the time-delay axis in (c) is cropped before 5 fs to enhance the features of the signal. The intensity axes for all the figures are normalized with respect to the signal with highest intensity for the sake of comparison. The UV pulse parameters are as follows: $E_U = 2.06 \times 10^{10}$ V/m, $\sigma_U = 1.2$ fs, $\omega_U = 4.76$ eV. The parameters for the first probe-pulse \mathcal{E}_0 and second probe-pulse \mathcal{E}_1 are as follows: $\sigma_0 = 0.9$ fs (FWHM = 2.12 fs), $\omega_X = 401$ eV, and $\sigma_1 = 1.7$ fs (FWHM = 4 fs).

11 shows the TRUECARs spectrum, which has been calculated using Eqs. 15 and 19. The TRUECARs spectra for the xx and yy components of the X-ray polarizability tensor, α_{xx} and α_{yy} are shown separately in Figs. 11(a) and (b) along with the sum of both components in Fig. 11(c). Note that the sum spectrum corresponds to a rotational averaged spectrum, which would be observed in a gas-phase experiment. The spectrum corresponding to α_{zz} is not shown here because it is five orders of magnitude weaker. The TRUECARs spectrum without the UV pump pulse has been subtracted from that of the prepared system with the UV pump pulse to remove the contribution from ground state vibrational Raman transitions.

The peak before 5 fs stems from the vibrational coherences created by the pump-pulse. At around 5-10 fs the wave packet reaches the CI region where the non-adiabatic couplings come into effect. Inspection of Figs. 11(a) and (b) shows an increase in intensity, indicating a build up of coherence.

Between 10 and 30 fs the effects of the CI can be seen in the spectrum. Both components in Figs. 11(a) and (b) show an increase in intensity. The xx component in Fig. 11(a) peaks between 10 and 20 fs and falls off at later times. The yy component in Fig. 11(b) also peaks

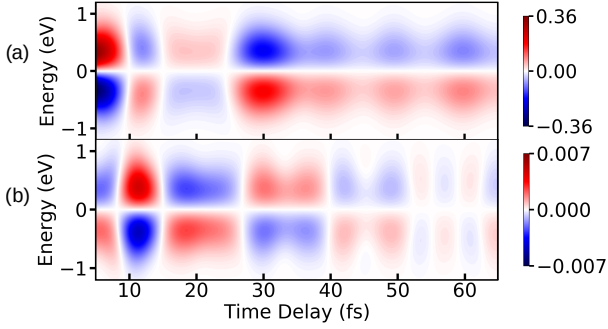


Figure 12. The TRUECARs signal for (a) vibrational coherence and (b) electronic coherence are shown. The intensity axes are normalized with respect to the TRUECARs signal in Fig. 11(a).

between 10 and 20 fs but has another strong peak at ≈ 30 fs. This increase can be explained as the build up in coherence as well as an increase in polarizability. The xx component of the polarizability of the $\pi\sigma^*$ peaks before the CI (at short NH bond distances) and goes to nearly zero after the wave packet has passed through the CI. The yy component shows the opposite behavior: it is near zero before the wave packet reaches the CI and peaks at larger NH bond distances. This explains the peak in Fig. 11(b) at 30 fs. The Stokes and anti-Stokes patterns of the spectra for the xx and yy components are out of phase, leading to a partial cancellation of the signal in Fig. 11(c). However, the oscillation patterns still have the same period. The strength of the TRUECARs signal depends on the magnitude of the matrix elements of the polarizability operator (see Eq. 19) along with the magnitude of the coherence generated. The diagonal elements of the polarizability operator constitute the vibrational coherence, while the off-diagonal elements constitute the electronic coherence in the spectrum. The TRUECARs spectra are constructed separately for the vibrational coherence and the electronic coherence to compare the effect on the overall signal. The TRUECARs signal corresponding to electronic coherence is shown in Fig. 12(b), and it has a maximum intensity around 10 fs which is the time-instance when the wave packets start reaching the CI. The TRUECARs signal corresponding to the vibrational coherence is shown in Fig. 12(a). Inspection of the polarizability matrix elements (see Eq. 19) also reveals that the diagonal elements are ≈ 2 times larger than the off-diagonal elements. Thus, the electronic coherences contribute significantly less than the vibrational coherences to the overall TRUECARs signal. Hence, the key signature of the CI, i.e. electronic coherence generation, is not clearly visible in the TRUECARs signal for pyrrole. Note that the vibrational and electronic degrees of freedom are strongly mixed in the

direct vicinity of the CI and thus one can not clearly distinguish between vibrational and electronic coherences.

After 30 fs the intensity of the signal decreases due to the dissociation. Note that this decay is mainly caused by absorption of the wave packet at the grid boundary (see Fig. 1). In these particular examples of the TRUECARs spectrum does not show the expected frequency resolution and time evolution of the energy gap between the valence states can not be visualized. This is mainly due to the choice of pulse parameters which are necessary to resolve the spectral features in the time domain.

VI. CONCLUSION

We have studied the CI in pyrrole using three different spectroscopy techniques, namely XAS, XSES, and TRUECARs. A set of transient XAS spectra was constructed by selecting the dominant states involved in the non-adiabatic dynamics (S_0 , $\pi\sigma^*$) and the transitions to the first nitrogen 1s core hole state. We could show that the signature of the CI in the spectrum consists of a resonance and an increase in signal intensity: For the lowest probe energy, the probe becomes resonant with the first core-hole state and a peak appears in the spectrum when the wave packet reaches the CI region. The transition dipole moment peaks in the vicinity of the CI leading to an increased absorption indicating the time it takes for the wave packet to reach the CI, allowing to narrow down the timing further. Due to the unbalanced branching of the wave packet at the CI, we see mainly the signature of the $\pi\sigma^*$ state in spectrum.

The time-resolved XSES spectrum was constructed using an X-ray probe-pulse, which has a frequency that is resonant with the valence-to-core transition corresponding to the CI region. The $\pi\sigma^*$ state and the C_1 state have a similar shape and thus a constant energy difference in the vicinity of CI. Consequently, the spontaneous emission peaks at a rather constant photon energy. In contrast to the XAS spectrum, the branching ratio at the CI is not a decisive factor. The spontaneous decay from the nitrogen 1s core hole state has a similar transition moment to S_0 and the $\pi\sigma^*$ state. As a result, one can now see a signature of the curve crossing in the XSES spectrum.

For the third technique we have constructed the TRUECARs signal. Here we explicitly probe the vibronic coherences that are generated in the molecule by means of a linear off-resonant Raman process. The TRUECARs signal depends on the X-ray transition polarizability and the magnitude of the electronic and vibrational coherences of the excited system. The simulated spectrum displays peaks between 10 fs and 20 fs which hint at non-adiabatic dynamics due to the CI. The spectra originating from the two polarizability ten-

sor components are out of phase and the overall signal is diminished. The spectral features correlate with the signatures of the XAS and XSES spectra putting the passage through the CI consistently between 10 fs and 20 fs. We note that the TRUECARS spectrum is dominated by the vibrational coherences and the increase of the polarizability near the CI rather than the electronic coherences.

In conclusion, we have shown that the existence of a CI in a molecule and its temporal appearance can be identified by a combination of multiple methods. Each technique on its own may deliver a spectrum that could potentially be difficult to interpret. The presented techniques probe different properties of the molecule and thus their combination gives a more complete picture.

We also note that the combination is also potential strategy to bypass the high demand on the pulse bandwidth to map out the rapidly changing energy near the CI. The pulses used in our simulations were longer than 1 fs thus explicitly avoiding attosecond pulses.

ACKNOWLEDGEMENTS

Support from the Swedish Research Council (Grant VR 2018-05346) is acknowledged.

DATA AVAILABILITY

The data is available on request from the authors.

-
- [1] Wolfgang Domcke, David R Yarkony, and Horst Köp-
pel. *Conical Intersections*. World Scientific, 2011.
 - [2] Michael Baer. *Beyond Born-Oppenheimer: electronic
nonadiabatic coupling terms and conical intersections*.
John Wiley & Sons, 2006.
 - [3] David R. Yarkony. Conical Intersections: Diaboli-
cal and Often Misunderstood. *Accounts Chem. Res.*,
31(8):511–518, 1998.
 - [4] M. Klessinger and J. Michl. *Excited States and Photo-
chemistry of Organic Molecules*. VCH, 1995.
 - [5] M. A. Robb, F. Bernardi, and M. Olivucci. Conical
intersections as a mechanistic feature of organic photo-
chemistry. *Pure and Applied Chemistry*, 67(5):783–789,
1995.
 - [6] Fernando Bernardi, Massimo Olivucci, and Michael A.
Robb. Potential energy surface crossings in organic photo-
chemistry. *Chem. Soc. Rev.*, 25:321–328, 1996.
 - [7] Yuan-Chung Cheng and Graham R. Fleming. Dynam-
ics of light harvesting in photosynthesis. *Annual Review
of Physical Chemistry*, 60(1):241–262, 2009. PMID:
18999996.
 - [8] Dario Polli, Piero Altoè, Oliver Weingart, Kate-
lyn M. Spillane, Cristian Manzoni, Daniele Brida,
Gaia Tomasello, Giorgio Orlandi, Philipp Kukura,
Richard A. Mathies, Marco Garavelli, and Giulio
Cerullo. Conical intersection dynamics of the pri-
mary photoisomerization event in vision. *Nature*,
467(7314):440–443, Sep 2010.
 - [9] Rajeshwar P. Sinha and Donat-P. Häder. Uv-induced
dna damage and repair: a review. *Photochem. Photo-
biol. Sci.*, 1:225–236, 2002.
 - [10] Mario Barbatti, Adélia J. A. Aquino, Jaroslav J. Szym-
czak, Dana Nachtigallová, Pavel Hobza, and Hans
Lischka. Relaxation mechanisms of uv-photoexcited
dna and rna nucleobases. *Proceedings of the National
Academy of Sciences*, 107(50):21453–21458, 2010.
 - [11] Wolfgang Domcke and David R. Yarkony. Role of
Conical Intersections in Molecular Spectroscopy and
Photoinduced Chemical Dynamics. *Annu. Rev. Phys.
Chem.*, 63(1):325–352, may 2012.
 - [12] Matthieu Sala and Dassia Egorova. Two-dimensional
photon-echo spectroscopy at a conical intersection: A
two-mode pyrazine model with dissipation. *Chem.
Phys.*, 481:206–217, dec 2016.
 - [13] Eric C. Wu, Qinghui Ge, Eric A. Arsenault,
Nicholas H.C. Lewis, Natalie L. Gruenke, Mar-
tin J. Head-Gordon, and Graham R. Fleming. Two-
dimensional electronic-vibrational spectroscopic study
of conical intersection dynamics: An experimental and
electronic structure study. *Phys. Chem. Chem. Phys.*,
21(26):14153–14163, jul 2019.
 - [14] Jindřich Krčmář, Maxim F. Gelin, Dassia Egorova, and
Wolfgang Domcke. Signatures of conical intersections
in two-dimensional electronic spectra. *J Phys. B-At.
Mol. Opt.*, 47(12):124019, jun 2014.
 - [15] N Breckwoldt, R Fung, R Sepehr, M Schmidt,
P Schwander, R Santra, and A Ourmazd. Single-
femtosecond atomic-resolution observation of a protein
1 traversing a conical intersection 2 3 4 A. *bioRxiv*, page
2020.11.13.382218, nov 2020.
 - [16] Hong Guang Duan, Ajay Jha, Xin Li, Vandana Tiwari,
Hanyang Ye, Pabitra K. Nayak, Xiao Lei Zhu, Zheng Li,
Todd J. Martinez, Michael Thorwart, and R. J. Dwayne
Miller. Intermolecular vibrations mediate ultrafast sin-
glet fission. *Sci. Adv.*, 6(38):52–70, sep 2020.
 - [17] Szymon Smolarek, Anouk M. Rijs, Wybren Jan Buma,
and Marcel Drabbels. Absorption spectroscopy of ade-
nine, 9-methyladenine, and 2-aminopurine in helium
nanodroplets. *Phys. Chem. Chem. Phys.*, 12(48):15600–
15606, dec 2010.
 - [18] Kewei Sun, Weiwei Xie, Lipeng Chen, Wolfgang Dom-
cke, and Maxim F. Gelin. Multi-faceted spectroscopic
mapping of ultrafast nonadiabatic dynamics near con-
ical intersections: A computational study. *J Chem.
Phys.*, 153(17):174111, nov 2020.
 - [19] M. C.E. Galbraith, S. Scheit, N. V. Golubev, G. Re-
itsma, N. Zhavoronkov, V. Despré, F. Lépine, A. I.
Kuleff, M. J.J. Vrakking, O. Kornilov, H. Köppel, and

- J. Mikosch. Few-femtosecond passage of conical intersections in the benzene cation. *Nat. Commun.*, 8(1), dec 2017.
- [20] H. J. Wörner, J. B. Bertrand, B. Fabre, J. Higuët, H. Ruf, A. Dubrouil, S. Patchkovskii, M. Spanner, Y. Mairesse, V. Blanchet, E. Mével, E. Constant, P. B. Corkum, and D. M. Villeneuve. Conical intersection dynamics in NO₂ probed by homodyne high-harmonic spectroscopy. *Sci. J.*, 334(6053):208–212, oct 2011.
- [21] Jens E. Bækhoj, Camille Lévêque, and Lars Bojer Madsen. Signatures of a conical intersection in attosecond transient absorption spectroscopy. *Phys. Rev. Lett.*, 121:023203, Jul 2018.
- [22] Yuki Kobayashi, Kristina F. Chang, Tao Zeng, Daniel M. Neumark, and Stephen R. Leone. Direct mapping of curve-crossing dynamics in IBr by attosecond transient absorption spectroscopy. *Sci. J.*, 364(6448):79–83, jul 2019.
- [23] Henry Timmers, Xiaolei Zhu, Zheng Li, Yuki Kobayashi, Mazyar Sabbar, Maximilian Hollstein, Maurizio Reduzzi, Todd J. Martínez, Daniel M. Neumark, and Stephen R. Leone. Disentangling conical intersection and coherent molecular dynamics in methyl bromide with attosecond transient absorption spectroscopy. *Nat. Commun.*, 10(1), dec 2019.
- [24] Thomas A.A. Oliver and Graham R. Fleming. Following Coupled Electronic-Nuclear Motion through Conical Intersections in the Ultrafast Relaxation of β -Apo-8'-carotenal. *J Phys. Chem. B*, 119(34):11428–11441, aug 2015.
- [25] Kristina S. Zinchenko, Fernando Ardana-Lamas, Isaka Seidu, Simon P. Neville, Joscelyn van der Veen, Valentina Utrio Lanfalconi, Michael S. Schuurman, and Hans Jakob Wörner. Sub-7-femtosecond conical-intersection dynamics probed at the carbon k-edge. *Sci. J.*, 371(6528):489–494, 2021.
- [26] Simon P. Neville, Majed Chergui, Albert Stolow, and Michael S. Schuurman. Ultrafast X-Ray Spectroscopy of Conical Intersections. *Phys. Rev. Lett.*, 120(24), jun 2018.
- [27] Kochise Bennett, Markus Kowalewski, and Shaul Mukamel. Nonadiabatic Dynamics May Be Probed through Electronic Coherence in Time-Resolved Photoelectron Spectroscopy. *J Chem. Theory Comput.*, 12(2):740–752, feb 2016.
- [28] Kochise Bennett, Markus Kowalewski, Jérémy R. Rouxel, and Shaul Mukamel. Monitoring molecular nonadiabatic dynamics with femtosecond X-ray diffraction. *P. Natl. Acad. Sci. USA*, 115(26):6538–6547, jun 2018.
- [29] Valérie Vallet, Zhenggang Lan, Susanta Mahapatra, Andrzej L. Sobolewski, and Wolfgang Domcke. Photochemistry of pyrrole: Time-dependent quantum wavepacket description of the dynamics at the $^1\pi\sigma^*-s_0$ conical intersections. *The Journal of Chemical Physics*, 123(14):144307, 2005.
- [30] Fabrizio Santoro, Carlo Petrongolo, and Alessandro Lami. Time- and frequency-resolved spontaneous emission: Theory and application to the NO₂ X2A'/A2A' conical intersection. *J Chem. Phys.*, 113(10):4073–4082, sep 2000.
- [31] Michael Y. Patuwo and Soo Y. Lee. Probing non-adiabatic conical intersections using absorption, spontaneous Raman, and femtosecond stimulated Raman spectroscopy. *J. Chem. Phys.*, 139(23):234101, dec 2013.
- [32] Ludger Inhester, Loren Greenman, Artem Rudenko, Daniel Rolles, and Robin Santra. Detecting coherent core-hole wave-packet dynamics in N₂ by time- and angle-resolved inner-shell photoelectron spectroscopy. *J. Chem. Phys.*, 151(5):054107, aug 2019.
- [33] U. Hergenhahn, O. Kugeler, A. Rüdél, E. E. Rennie, and A. M. Bradshaw. Symmetry-selective observation of the N 1s shape resonance in N₂. *J Phys. Chem. A*, 105(23):5704–5708, jun 2001.
- [34] M. S. Schöffler, J. Titze, N. Petridis, T. Jahnke, K. Cole, L. Ph H. Schmidt, A. Czasch, D. Akoury, O. Jagutzki, J. B. Williams, N. A. Cherepkov, S. K. Semenov, C. W. McCurdy, T. N. Rescigno, C. L. Cocke, T. Osipov, S. Lee, M. H. Prior, A. Belkacem, A. L. Landers, H. Schmidt-Böcking, Th Weber, and R. Dörner. Ultrafast probing of core hole localization in N₂. *Sci. J.*, 320(5878):920–923, may 2008.
- [35] Weijie Hua, Sven Oesterling, Jason D. Biggs, Yu Zhang, Hideo Ando, Regina de Vivie-Riedle, Benjamin P. Fingerhut, and Shaul Mukamel. Monitoring conical intersections in the ring opening of furan by attosecond stimulated X-ray Raman spectroscopy. *Struct. Dynam. US*, 3(2), mar 2016.
- [36] Daeheum Cho and Shaul Mukamel. Stimulated X-ray Raman Imaging of Conical Intersections. *J. Phys. Chem. Lett.*, 11(1):33–39, jan 2020.
- [37] Yu Zhang, Jason D. Biggs, Weijie Hua, Konstantin E. Dorfman, and Shaul Mukamel. Three-dimensional attosecond resonant stimulated X-ray Raman spectroscopy of electronic excitations in core-ionized glycine. *Phys. Chem. Chem. Phys.*, 16(44):24323–24331, oct 2014.
- [38] Markus Kowalewski, Kochise Bennett, Konstantin E. Dorfman, and Shaul Mukamel. Catching Conical Intersections in the Act: Monitoring Transient Electronic Coherences by Attosecond Stimulated X-Ray Raman Signals. *Phys. Rev. Lett.*, 115(19):193003, nov 2015.
- [39] Daniel Keefer, Thomas Schnappinger, Regina de Vivie-Riedle, and Shaul Mukamel. Visualizing conical intersection passages via vibronic coherence maps generated by stimulated ultrafast X-ray Raman signals. *P Natl. Acad. Sci. USA*, 117(39):24069–24075, sep 2020.
- [40] Daeheum Cho, Jérémy R. Rouxel, and Shaul Mukamel. Stimulated X-ray Resonant Raman Spectroscopy of Conical Intersections in Thiophenol. *J Phys. Chem. Lett.*, 11(11):4292–4297, jun 2020.
- [41] Frank Anel III, K. C. Hasson, Feng Gai, Philip A. Anfinrud, and Richard A. Mathies. Femtosecond time-resolved spectroscopy of the primary photochemistry of phytochrome. *Biospectroscopy*, 3(6):421–433, 1997.
- [42] Gerd G Kochendoerfer and Richard A Mathies. Spontaneous emission study of the femtosecond isomerization dynamics of rhodopsin. *J. Phys. Chem.*, 100(34):14526–14532, 1996.
- [43] David A. Blank, Simon W. North, and Yuan T. Lee. The ultraviolet photodissociation dynamics of pyrrole.

- Chemical Physics*, 187(1):35–47, 1994.
- [44] A. L. Sobolewski, W. Domcke, C. Dedonder-Lardeux, and C. Jouvet. Excited-state hydrogen detachment and hydrogen transfer driven by repulsive $^1\pi\sigma^*$ states: A new paradigm for nonradiative decay in aromatic biomolecules. *Phys. Chem. Chem. Phys.*, 4:1093–1100, 2002.
 - [45] J. Wei, A. Kuczmanski, J. Riedel, F. Renth, and F. Temps. Photofragment velocity map imaging of h atom elimination in the first excited state of pyrrole. *Phys. Chem. Chem. Phys.*, 5:315–320, 2003.
 - [46] J. Wei, J. Riedel, A. Kuczmanski, F. Renth, and F. Temps. Photodissociation dynamics of pyrrole: Evidence for mode specific dynamics from conical intersections. *Faraday Discuss.*, 127:267–282, 2004.
 - [47] Kateryna Grygoryeva, Jozef Rakovský, Ivo S. Vinklár, Ondřej Votava, Michal Fárnik, and Viktoriya Poterya. Vibrationally mediated photodissociation dynamics of pyrrole. *AIP Advances*, 9(3):035151, 2019.
 - [48] Michael N. R. Ashfold, Graeme A. King, Daniel Muddock, Michael G. D. Nix, Thomas A. A. Oliver, and Alan G. Sage. $\pi\sigma^*$ excited states in molecular photochemistry. *Phys. Chem. Chem. Phys.*, 12:1218–1238, 2010.
 - [49] P. A. Mullen and M. K. Orloff. Ultraviolet absorption spectrum of pyrrole vapor including the observation of low-energy transitions in the far ultraviolet. *The Journal of Chemical Physics*, 51(5):2276–2278, 1969.
 - [50] C. D. Cooper, A. D. Williamson, John C. Miller, and R. N. Compton. Resonantly enhanced multiphoton ionization of pyrrole, n-methyl pyrrole, and furan. *The Journal of Chemical Physics*, 73(4):1527–1537, 1980.
 - [51] Michael H. Palmer, Isobel C. Walker, and Martyn F. Guest. The electronic states of pyrrole studied by optical (vuv) absorption, near-threshold electron energy-loss (eel) spectroscopy and ab initio multi-reference configuration interaction calculations. *Chemical Physics*, 238(2):179–199, 1998.
 - [52] Jian Wan, Jaroslav Meller, Masahiko Hada, Masahiro Ehara, and Hiroshi Nakatsuji. Electronic excitation spectra of furan and pyrrole: Revisited by the symmetry adapted cluster–configuration interaction method. *The Journal of Chemical Physics*, 113(18):7853–7866, 2000.
 - [53] Paolo Celani and Hans-Joachim Werner. Analytical energy gradients for internally contracted second-order multireference perturbation theory. *The Journal of Chemical Physics*, 119(10):5044–5057, 2003.
 - [54] Mario Barbatti, Mario Vazdar, Adélia J. A. Aquino, Mirjana Eckert-Maksić, and Hans Lischka. The nonadiabatic deactivation paths of pyrrole. *The Journal of Chemical Physics*, 125(16):164323, 2006.
 - [55] M. N. R. Ashfold, B. Cronin, A. L. Devine, R. N. Dixon, and M. G. D. Nix. The role of $\pi\sigma^*$ excited states in the photodissociation of heteroaromatic molecules. *Science*, 312(5780):1637–1640, 2006.
 - [56] Brid Cronin, Michael G. D. Nix, Rafay H. Qadiri, and Michael N. R. Ashfold. High resolution photofragment translational spectroscopy studies of the near ultraviolet photolysis of pyrrole. *Phys. Chem. Chem. Phys.*, 6:5031–5041, 2004.
 - [57] Mahesh Gudem and Markus Kowalewski. Controlling the photostability of pyrrole with optical nanocavities. *The Journal of Physical Chemistry A*, 0(0):null, 0. PMID: 33464084.
 - [58] Guorong Wu, Simon P. Neville, Oliver Schalk, Taro Sekikawa, Michael N. R. Ashfold, Graham A. Worth, and Albert Stolow. Excited state non-adiabatic dynamics of pyrrole: A time-resolved photoelectron spectroscopy and quantum dynamics study. *The Journal of Chemical Physics*, 142(7):074302, 2015.
 - [59] S. P. Neville and G. A. Worth. A reinterpretation of the electronic spectrum of pyrrole: A quantum dynamics study. *The Journal of Chemical Physics*, 140(3):034317, 2014.
 - [60] Hiroyuki Shimada, Taishi Fukao, Hirotake Minami, Masatoshi Ukai, Kentaro Fujii, Akinari Yokoya, Yoshihiro Fukuda, and Yuji Saitoh. Nitrogen K-edge X-ray absorption near edge structure (XANES) spectra of purine-containing nucleotides in aqueous solution. *J. Chem. Phys.*, 141(5):055102, aug 2014.
 - [61] Anna Nissen, Hans O Karlsson, and Gunilla Kreiss. A perfectly matched layer applied to a reactive scattering problem. *J. Chem. Phys.*, 133(5):054306, 2010.
 - [62] Konstantin E. Dorfman, Frank Schlawin, and Shaul Mukamel. Nonlinear optical signals and spectroscopy with quantum light. *Rev. Mod. Phys.*, 88(4):045008, dec 2016.
 - [63] Shaul Mukamel and Saar Rahav. Ultrafast nonlinear optical signals viewed from the molecule’s perspective: Kramers–heisenberg transition-amplitudes versus susceptibilities. In *Adv. Atom. Mol. Opt. Phys.*, volume 59, pages 223–263. Elsevier, 2010.
 - [64] Konstantin E Dorfman, Kochise Bennett, and Shaul Mukamel. Detecting electronic coherence by multidimensional broadband stimulated x-ray Raman signals. *Phys. Rev. A*, 92:23826, 2015.
 - [65] S. Mukamel. *Principles of Nonlinear Optical Spectroscopy*. Oxford series in optical and imaging sciences. Oxford University Press, 1999.
 - [66] Markus Kowalewski, Benjamin P Fingerhut, Konstantin E Dorfman, Kochise Bennett, and Shaul Mukamel. Simulating Coherent Multidimensional Spectroscopy of Nonadiabatic Molecular Processes: From the Infrared to the X-ray Regime. *Chem. Rev.*, 117(19):12165–12226, 2017.
 - [67] Ph V Demekhin and LS Cederbaum. Resonant auger decay of core-excited co molecules in intense x-ray laser pulses: the o ($1s \rightarrow \pi^*$) excitation. *J. Phys. B-At. Mol. Opt. Physics*, 46(16):164008, 2013.
 - [68] Thomas JA Wolf, Alexander C Paul, Sarai D Folkestad, Rolf H Myhre, James P Cryan, Nora Berrah, Phil H Bucksbaum, Sonia Coriani, Giacomo Coslovich, Raimund Feifel, et al. Transient resonant auger-meitner spectra of photoexcited thymine. *arXiv preprint arXiv:2009.14355*, 2020.
 - [69] Kochise Bennett, Markus Kowalewski, and Shaul Mukamel. Probing electronic and vibrational dynamics in molecules by time-resolved photoelectron, auger-electron, and x-ray photon scattering spectroscopy. *Faraday Discuss.*, 177:405–428, 2015.

- [70] D C Haynes, M Wurzer, A Schletter, A Al-Haddad, C Blaga, C Bostedt, J Bozek, H Bromberger, R Kienberger, A R Maier, T Maxwell, T Mazza, M Meyer, H Park, J Robinson, C Roedig, H Schlarb, R Singla, F Tellkamp, P A Walker, K Zhang, G Doumy, C Behrens, and A L Cavalieri. Clocking Auger electrons. *Nat. Phys.*, 12:21.
- [71] Göran Wendin. Anomalous X-Ray Scattering. *Phys. Scripta*, 21(3-4):535–542, jan 1980.
- [72] Christoph A Marx, Upendra Harbola, and Shaul Mukamel. Nonlinear optical spectroscopy of single, few, and many molecules: Nonequilibrium green’s function approach. *Phys. Rev. A*, 77(2):022110, 2008.
- [73] Peter F Bernath. *Spectra of atoms and molecules*. Oxford university press, 2020.
- [74] H.-J. Werner, P. J. Knowles, G. Knizia, F. R. Manby, and M. Schütz. Molpro: a general-purpose quantum chemistry program package. *WIREs Comput. Mol. Sci.*, 2:242–253, 2012.
- [75] H.-J. Werner, P. J. Knowles, G. Knizia, F. R. Manby, M. Schütz, O. Celani, W. Györffy, D. Kats, T. Korona, R. Lindh, et al. Molpro, version 2019.2, a package of ab initio programs, 2019.
- [76] Markus Kowalewski and Shaul Mukamel. Stimulated Raman signals at conical intersections: Ab initio surface hopping simulation protocol with direct propagation of the nuclear wave function. *J. Chem. Phys.*, 143(4):044117+, 2015.
- [77] W. E. Arnoldi. The principle of minimized iterations in the solution of the matrix eigenvalue problem. *Q. Appl. Math.*, 9(1):17–29, apr 1951.